

From Fractional Quantum Anomalous Hall Smectics to Polar Smectic Metals: Nontrivial Interplay Between Electronic Liquid Crystal Order and Topological Order in Correlated Topological Flat Bands

Hongyu Lu,^{1,*} Han-Qing Wu,^{2,*} Bin-Bin Chen,^{1,†} Kai Sun,^{3,‡} and Zi Yang Meng^{1,§}

¹*Department of Physics and HKU-UCAS Joint Institute of Theoretical and Computational Physics, The University of Hong Kong, Pokfulam Road, Hong Kong SAR, China*

²*Guangdong Provincial Key Laboratory of Magnetoelectric Physics and Devices, School of Physics, Sun Yat-sen University, Guangzhou 510275, China*

³*Department of Physics, University of Michigan, Ann Arbor, Michigan 48109, USA*
(Dated: January 2, 2024)

Abstract Integer or fractional quantum Hall crystals, states postulating the coexistence of charge order with integer or fractional quantum Hall effect, have long been proposed in theoretical studies in Landau levels [1–6]. Inspired by recent experiments on integer or fractional quantum anomalous Hall (IQAH/FQAH) states in MoTe₂ [7–10] and rhombohedral multilayer graphene [11], this work examines the archetypal correlated flat band model on a checkerboard lattice at filling $\nu = 2/3$. Interestingly, at this filling level, we find that this topological flatband does not stabilize conventional FQAH states. Instead, the unique interplay between smectic charge order and topological order gives rise to two intriguing quantum states. As the interaction strength increases, the system first transitions from a Fermi liquid into FQAH smectic (FQAHS) states, where FQAH topological order coexists cooperatively with smectic charge order. With a further increase in interaction strength, the system undergoes another quantum phase transition and evolves into a polar smectic metal. Contrary to conventional smectic order and FQAHS states, this gapless state spontaneously breaks the two-fold rotational symmetry, resulting in a nonzero electric dipole moment and ferroelectric order. In addition to identifying the ground states, large-scale numerical simulations are also used to study low-energy excitations and thermodynamic characteristics. We find that FQAHS states exhibit two distinct temperature scales: the onset of charge order and the onset of the fractional Hall plateau, respectively. Interestingly, the latter is dictated by charge-neutral low-energy excitations with finite momenta, known as magnetorotons. Our studies suggest that these nontrivial phenomena could, in principle, be accessed in future experiments with moiré systems.

Introduction

The interplay between charge order and topological order has been a focal point in the study of Landau levels and the quantum Hall effects, both integer and fractional. Traditionally, they are perceived as competing orders, because they're governed by different physics principles – Landau's symmetry-breaking paradigm for the former and topologically nontrivial quantum wavefunctions for the latter. However, these two distinct types of orders can also coexist cooperatively, as theoretical studies have shown [1–3]. Over the past thirty years, extensive research has been devoted to investigate such coexistence phases, both theoretically [4–6, 12–16] and experimentally [17–25], where charge order and topological order strongly intertwine together. Based on their symmetry-breaking patterns, such intertwined states can be classified into three main categories: the integer and fractional quantum Hall nematic (IQHN and FQHN) states, smectic (IQHS and FQHS) states, and crystal (IQHC and FQHC) states, where a nematic state spontaneously breaks only the rotational symmetry, a smectic state breaks the rotational symmetry as well as the translational symmetry along one spatial direction (i.e., a unidirectional stripe), and a crystal state breaks the 2D translational symmetry.

Parallel to Landau level systems, integer and fractional quantum anomalous Hall (IQAH and FQAH) states at *zero magnetic field* – known as integer and fractional Chern insulators – have been proposed [26–29] and realized [7–11, 30]. Similar to Landau levels, the competition between charge or

der and topological order frequently emerges in the strong coupling regime of Chern bands. However, can charge orders and IQAH/FQAH effects exist cooperatively?

Theoretically, such coexisting states are feasible, and these intertwined orders might even play a crucial role in the FQAH states observed in recent experiments [7–11]. Theoretical studies of FQAH states in twisted MoTe₂ bilayers [31–38] identified the significance of remote bands that break the particle-hole symmetries [35, 36], and postulated the potential interplay of the competing CDW order with the FQAH state [35–37, 39, 40]. In rhombohedral pentalayer graphene/hBN moiré superlattices, it is proposed that the narrow $C = -1$ Chern band can exhibit interaction-driven spontaneously time-reversal and translational symmetry breaking, which are stable even without moiré potential and can give rise to IQAHC state [41–43]. FQAHC and possible FQAH-CDW phase transitions has also been proposed [39, 44]. For a $C = -1$ crystal at fractional filling, FQAH states are observed in exact diagonalization simulations, utilizing projected Hamiltonian to the flat Chern bands [41, 42].

Although the concept appears theoretically sound, our understanding of these intertwined charge and topological orders at a microscopic level is very limited. For crystal order that breaks 2D translational symmetries, its coexistence with topological order are found in a triangular lattice model referred to as the topological pinball liquid [45]. However, for microscopic models where FQAH effects coexist with smectic orders, our knowledge is essentially non-existent. Further-

more, a more critical challenge for such intertwined states lies in understanding their thermodynamic properties at finite temperatures — a largely uncharted territory in both theoretical and numerical studies. The primary obstacle stems from the absence of unbiased theoretical and numerical tools capable of providing reliable predictions at finite temperatures. Considering that experimental studies are exclusively conducted at finite temperatures, such theoretical knowledge is of paramount importance.

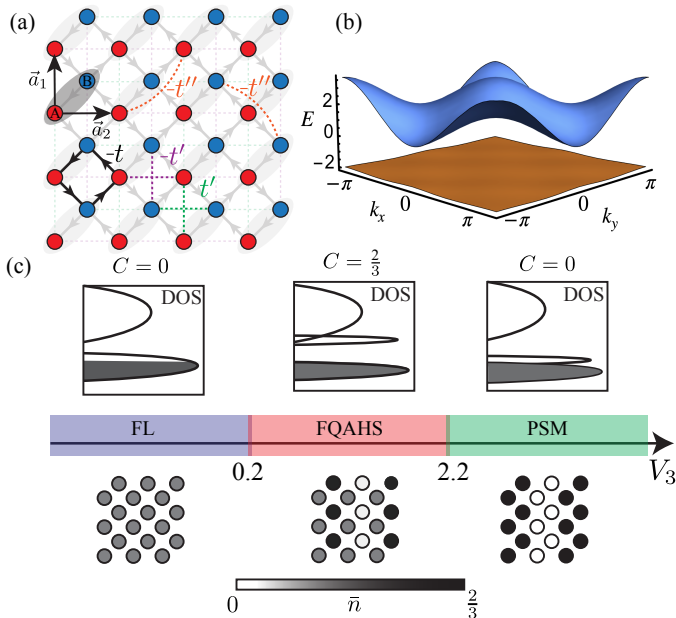


FIG. 1. **Model and phase diagram.** (a) Checkerboard lattice the lattice primitive vectors $\mathbf{a}_1 = (0, 1)$, $\mathbf{a}_2 = (1, 0)$. Different hoppings are denoted by different colors and the arrows represent the directions of the loop current. (b) The band dispersion of the tight-binding Hamiltonian, with the lower band nearly flat. (c) Phase diagram at $\nu = 2/3$ as NNNN interaction strength V_3 is varied. FL represents a C_4 -symmetric Fermi liquid state with uniform charge distribution, and FQAHS represents a fractional quantum anomalous Hall smectic state with gapped bulk, a unidirectional stripe order and Chern number $C = 2/3$, and PSM represents a polar smectic metal phase with a ferroelectric stripe order.

In this Letter, we study intertwined charge and topological orders using the archetypal correlated topological flat-band model on a checkerboard lattice [27, 28, 46]. In addition to conventional numerical methods, density matrix renormalization group (DMRG) and exact diagonalization (ED), to study the thermodynamic properties, we also utilize the state-of-the-art tensor network technique, exponential tensor renormalization group (XTRG), which has been found in recent studies to be a highly efficient and reliable method to reveal finite-temperature properties of FQAH systems [46]. Unlike previous studies which primarily focused on low fillings, our attention is focused on higher fillings with $\nu = 2/3$, where we observed highly intriguing interplays between smectic charge orders (unidirectional charge stripes) and topological order:

1. As interaction strength is increased, the Fermi liquid (FL) state transitions into a FQAH smectic (FQAHS) state, and subsequently to a polar smectic metal state [Fig. 1(c)].
2. The FQAHS state is gapped and has a fractional Hall conductivity of $\sigma_{xy} = \nu = 2/3$. Its smectic ordering wavevector, either $(\pi, 0)$ or $(0, \pi)$, spontaneously breaks the four-fold rotational symmetry down to two-fold symmetry. This charge order also breaks the lattice translational symmetry along the direction of the wavevector. On a torus, this state displays a 12-fold ground state degeneracy, with factor 3 from topological degeneracy and factor 4 from the rotational and translational symmetry breaking [Figs. 1(c), 2 (b), and 3].
3. The thermodynamics of the FQAHS state reveal three distinct temperature/energy scales: (1) the onset temperature of the fractionalized Hall plateau T^* , (2) the critical temperature of the stripe order T_c , and (3) the charge gap of this incompressible state T_{cg} . XTRG simulations suggest $T^* \ll T_c \ll T_{cg}$. Around and below T^* , the dominant fluctuations are charge-neutral magnetorotons. However, around T_c , fluctuations of the charge order become the principal fluctuations, whose wavevector differs significantly from the rotons [Fig. 4].
4. The polar smectic metal is a compressible liquid. This smectic order shares the same ordering wave vector with FQAHS, but it breaks an additional symmetry (two-fold rotation), making the ground state degeneracy (arising from spontaneous symmetry breaking) 8-fold [Fig. 1(c)].

In classical liquid crystals, a comparable state to this polar smectic is known as the uniaxial ferroelectric smectic A phase (SmA_F), recently identified in polar molecule systems [47]. The polar smectic metallic phase we find here serves as a quantum counterpart of that state. Unlike classical systems, our polar smectic state develops in a system devoid of any polar building blocks. Interestingly, the melting of this polar smectic order (upon reducing interaction strength) is highly nontrivial. Instead of directly transitioning into the disordered phase, the system first turns into a regular smectic state, thereby restoring part of the broken symmetries (two-fold rotation). This two-step transition process strongly echoes the phenomena of vestigial order [48–52].

Results

Model and Phase Diagram We consider a two-band spinless fermion model on the checkerboard lattice,

$$\begin{aligned}
 H = & - \sum_{\langle i,j \rangle} t e^{i\phi_{ij}} (c_i^\dagger c_j + h.c.) - \sum_{\langle\langle i,j \rangle\rangle} t'_{ij} (c_i^\dagger c_j + h.c.) \\
 & - \sum_{\langle\langle\langle i,j \rangle\rangle\rangle} t'' (c_i^\dagger c_j + h.c.) + \sum_{\langle\langle\langle i,j \rangle\rangle\rangle} V_3 (n_i - \frac{1}{2})(n_j - \frac{1}{2})
 \end{aligned} \tag{1}$$

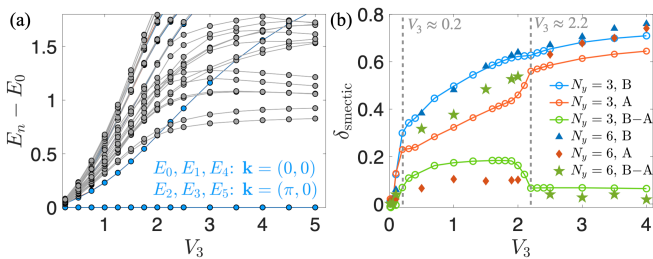


FIG. 2. Determination of phase boundaries via ED and DMRG. (a) $3 \times 6 \times 2$ ED spectra with changing V_3 . The blue lines/dots marks the 6-fold degenerate ground states in FQAHs phase for $0.2 < V_3 < 2.2$. (b) The charge-stripe order parameters of A and B sublattices measured via DMRG for cylinders with width $N_y = 3$ and $N_y = 6$. The difference between $\delta_{\text{smectic}}^A$ and $\delta_{\text{smectic}}^B$ is also plotted, and the two grey dashed lines label the phase boundaries.

with nearest-neighbor (NN, t), next-nearest-neighbor (NNN, t'), and next to next nearest-neighbor (NNNN, t'') hoppings, and NNNN repulsive interaction (V_3), as shown in Fig. 1 (a). The tight-binding parameters are: $t = 1$ (as the energy unit), $t'_{ij} = \pm 1/(2 + \sqrt{2})$ with alternating sign in edge-sharing plaquettes, $t'' = -1/(2 + 2\sqrt{2})$ and $\phi_{ij} = \frac{\pi}{4}$ along the direction of the arrows, such that the relationship between the flat-band width W , the gap between the flat and remote band Δ are $W (= 0.08) \ll \Delta (= 2.34)$, as shown in Fig. 1(b). And due to the flux in each plaquette, the tight-binding model acquires opposite Chern number $C = \pm 1$ for the flat and remote bands [28].

Previous research on this model has confirmed the existence of FQAH states at $\nu = 1/3$ and $\nu = 1/5$. No competing CDW order was noted, even when the interaction surpassed the band gap Δ [28, 46]. However, the phenomena at fillings of $1/2 < \nu < 1$ have largely been left unexplored. In contrast to the first Landau level, where fillings $\nu < 1/2$ and $\nu > 1/2$ are simply connected by the particle-hole symmetry, a general Chern band does not display such symmetry. Consequently, the repulsive interaction and the existence of a remote band result in significantly different physics for $\nu > 1/2$ compared to the $\nu < 1/2$ regime. As will be demonstrated below, we observe a highly nontrivial interplay between charge order and topological order for $\nu > 1/2$, which was absent in the $\nu < 1/2$ regime.

We focus on $\nu = 2/3$. Temporarily, our simulations observe no topological order for NN and NNN interactions (not shown), and thus here we focus on the NNNN interaction V_3 , leaving global phase diagram for future study. At the strong coupling limit, $V_3 \rightarrow \infty$, the minimization of potential energy leads to a unidirectional stripe order as shown in Fig. 1(c), polar smectic metal (PSM), where sites represented by circle always remain empty and particles only occupy sites of filled disks. In this charge configuration, particles never occupies any pair of NNNN sites and thus minimize the potential energy. This state is an electronic smectic state [53]. Remarkably, this smectic state is a unique kind. In direct contrast to typical electronic smectic state, which is invariant under C_2

rotation along the direction perpendicular to the x-y plane, this smectic spontaneously breaks this two-fold rotational symmetry. This additional symmetry breaking increase the number of degenerate ground state charge configuration by a factor of 2. More importantly, it implies that this charge ordered state has a spontaneously-generated in-plane electric dipole (perpendicular to the stripes), i.e., it is a ferroelectric state. To highlight this ferroelectric order, below, we will call this charge order the polar smectic order. As for physical properties of this charge ordered state, because sites of filled disks are only partially occupied with an average density $\nu = 2/3$, in principle electrons can move along the stripes and tunnel between the stripes. Such a system can be characterized as coupled Luttinger liquids. Depending on the Luttinger parameters and the inter-stripe couplings, various phases might be stabilized, such as smectic superconductor, smectic crystal (insulator), smectic metal, and Fermi liquid [54].

In our simulation, this polar smectic charge order is indeed observed at $V_3 > 2.2$. In our simulations, as will be shown in later parts, we find this state to be gapless/conducting, suggesting either a polar smectic metal or a polar Fermi liquid. In Fig. 2(a), we plot the energy spectra of a $3 \times 6 \times 2$ torus obtained from ED [other system sizes are shown in Supplemental Material (SM) [55]], and the smectic order parameter is calculated using DMRG on cylinders of width of $N_y = 3$ and $N_y = 6$ [Fig. 2 (b)]. Here we define two smectic order parameters, for A- and B- sublattices respectively, $\delta_{\text{smectic}}^{A/B} = \frac{2}{N'} \sum_i (-1)^{x_i} n_{\mathbf{r}_i}^{A/B}$ with summation over a few unit cells i 's in the bulk and N' being the number of such sites. The integer x_i is x coordinate of the i th unit cell (along the cylinder). In the polar smectic phase, both the two order parameters (for A- and B- sublattices) shall take nonzero expectation values, and at $V_3 \rightarrow \infty$, their values saturate to $\nu = 2/3$ as expected. It is worthwhile noting that in our DMRG simulations, the stripe pattern is found to be along the y axis for the cylindrical geometry, but in the thermodynamic limit, the orientation of the stripes can be either along x or y , determined by spontaneous symmetry breaking.

As we reduces V_3 , quantum fluctuations start to melt the polar smectic order. However, instead of a direct transition to a homogenous phase, we find an intermediate phase for $0.2 < V_3 < 2.2$. As shown in Fig. 2(b), δ^B remains nonzero and large, while δ^A becomes very small. More importantly, the value of δ^A reduces dramatically as we increase the system size (from $N_y = 3$ to 6), indicating that the small nonzero value of δ^A is a finite size effect, which will vanish in the thermodynamic limit. This phase of $\delta^B \neq 0$ and $\delta^A = 0$ is a non-polar smectic order, fundamentally different from the polar smectic order. Although it shares the same ordering wavevector $(\pi, 0)$ with the polar smectic order, the two-fold rotational symmetry is recovered and thus the in-plane electric dipole moment reduces to zero. In other words, this smectic phase at $V < 2.2$ doesn't exhibit ferroelectric order. More importantly, this intermediate smectic phase has a nontrivial topological order. It is a gapped FQAH state with Hall conductivity $\sigma_{xy} = \nu = 2/3$.

Upon further reducing V_3 , this nonpolar smectic order is eventually melted for $V_3 < 0.2$, where the smectic FQAH state gives its way to a homogenous and isotropic Fermi liquid phase. The changes of charge order parameters are discontinuous around transition points.

These phase diagram is one of the key result of this study, which is summarize in Fig. 1. To the best of our knowledge, such a coexistence phase of the FQAH effect and smectic order has not yet been directly observed in microscopic models. Neither does the competition between a non-polar FQAH smectic phase and polar electronic smectic order. In the following sections, we will present more numerical evidence to support this phase diagram, as well as thermodynamic characteristics of these nontrivial quantum phases.

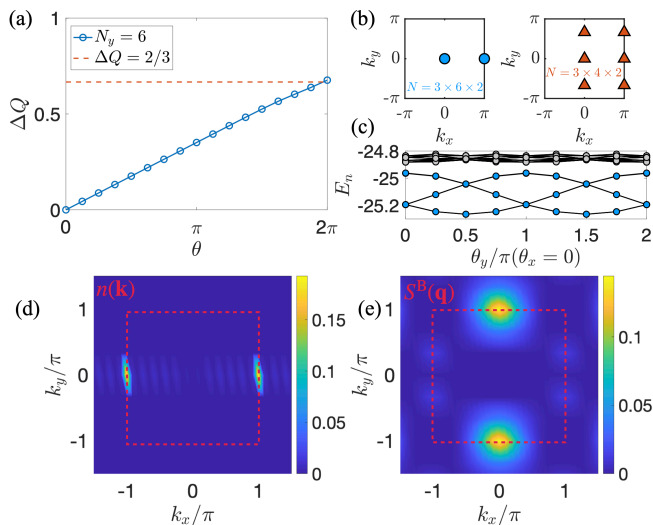


FIG. 3. **Ground-state properties of FQAHs.** (a) Charge pumping from DMRG and $\Delta Q \approx 2/3$. (b) The momentum sectors of the 6-fold degenerate ground states on toruses of sizes $N = 3 \times 6 \times 2$ and $N = 3 \times 4 \times 2$. (c) Energy spectrum flow of FQAHs ground states at $V_3 = 1$ using a $3 \times 6 \times 2$ torus with twist boundary condition along a_1 direction. (d) DMRG result of density distribution $n(\mathbf{k})$ and (e) structure factor $S^B(\mathbf{q})$ in a $N_y = 6$ cylinder at $V_3 = 1$.

FQAHs state In this section, we set $V_3 = 1$ and scrutinize the topological properties and thermodynamics of the FQAHs phase. The Hall conductivity is directly measured through charge pumping in DMRG simulations. As we adiabatically introduce a 2π magnetic flux ($c_i^\dagger c_j + h.c. \rightarrow c_i^\dagger c_j e^{i\theta} + h.c.$) for hopping across the periodic boundary in a cylinder of width $N_y = 6$, we find two thirds of an electron charge being pumped from one edge of the cylinder to the opposite one, signifying a fractional Hall conductivity of $\sigma_{xy} = 2/3$ [Fig. 3(a)].

ED simulations provide further corroboration for this conclusion, revealing six-fold degenerate ground states as depicted in Fig. 3(b) and (c), as well as in the SM [55]. With twisted boundary conditions, we find that each ground state possesses a fractional Chern number $C = 2/3$. For a $N = 3 \times 6 \times 2$ torus, three ground states are located at $(0, 0)$

and the remainder at $(\pi, 0)$. For a $N = 3 \times 4 \times 2$ cluster, these states can be found at $(0, 2m\pi/3)$ and $(\pi, 2m\pi/3)$ with $m = -1, 0, 1$. This ground state degeneracy and corresponding momentum sectors are in full alignment with the coexistence states of FQAH and non-polar smectic order. The six-fold ground states can be attributed to the combined effects of translational-symmetry-breaking leading to a 2-fold degeneracy for the ordering wavevector $\mathbf{Q} = (\pi, 0)$ and 3-fold topological degeneracy for a FQAH state with $C = 2/3$ on a torus. Notably, because the geometry of these ED clusters are incompatible with horizontal stripes, stripes observed here are only along the y direction. In the thermodynamic limit, stripes along x would further double the ground state degeneracy by a factor of 2. Also, it's noteworthy to mention that the observed six-fold ground state degeneracy implies a non-polar smectic order, as a polar smectic would yield a 12-fold degeneracy due to the four degenerate charge patterns for stripes along y as illustrated in the SM, confirming the ground state charge pattern previously discussed based on order parameter measurements using DMRG.

For various ED clusters, we observe that the momentum sectors of ground states consistently display this structure: three ground states are located at momentum $(K_x^{(i)}, K_y^{(i)})$ with $i = 1, 2, 3$, in accordance with the anticipated momentum sectors of FQAH states without charge order, while the remaining three has momentum $(K_x^{(i)}, K_y^{(i)}) + (\pi, 0)$. This observation further affirms the charge pattern and its coexistence with topological order. For vertical stripes in the thermodynamic limit, any FQAH ground state ψ_{FQAH} coexists with a degenerate state, $T_x \psi_{\text{FQAH}}$, where T_x is a translation operator shifting the system along the x -axis by one lattice constant. For ED simulations on a finite-sized torus, these two degenerate ground states hybridize and their superpositions result in two nearly degenerate states with total momentum (K_x, K_y) and $(K_x, K_y) + (\pi, 0)$ respectively.

Besides coexistence of charge and topological orders, this FQAHs state also exhibits nontrivial quantum fluctuations. As shown in Fig. 3(d), the k -space charge density, $n(\mathbf{k})$, acquired from DMRG for a $N_y = 6$ cylinder, reveals a sharp peak at $(\pi, 0)$, thereby verifying the smectic order. Within the same simulation, a peak in the density-density correlation function, $S^{A/B}(\mathbf{q}) = \sum_j e^{-i\mathbf{q}(\mathbf{r}_0 - \mathbf{r}_j)} (\langle n_0^{A/B} n_j^{A/B} \rangle - \langle n_0^{A/B} \rangle \langle n_j^{A/B} \rangle)$, is noted at $(0, \pi)$ [See Fig. 3(e)]. This correlation function peak does not arise from the smectic order as it is situated at a completely different k point. Instead, it suggests that low-energy charge-neutral fluctuations are dominated by excitations with a finite momentum $\mathbf{q} \sim (0, \pi)$, also referred to as magnetorotons, analogous to similar excitations observed in FQAH states without charge orders [46].

Furthermore, we study the thermodynamics via XTRG of the FQAH state with $V_3 = 1$ in a $3 \times 12 \times 2$ cylinder and we show the specific heat, compressibility, and smectic order parameter and structure factor of B sublattice in Fig. 4 (a,b), with $S^B(\mathbf{q})$ at different temperature in Fig. 4 (c,d). Here, we find three different temperature scales. The gap of charge ex-

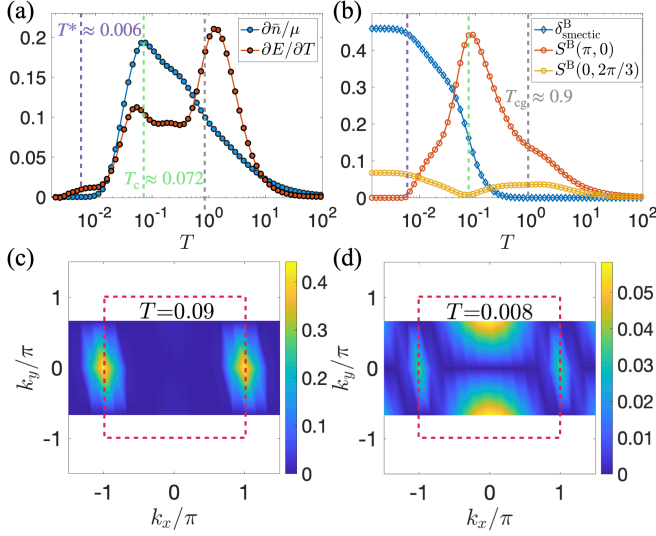


FIG. 4. **Thermodynamics of the FQAH state at $V_3 = 1$.** (a) Specific heat and compressibility, and (b) structure factors and charge-smectic order parameters of B sublattice versus temperature. (c,d) Structure factors plotted at $T = 0.09$ and $T = 0.008$ respectively. The dashed lines in (a) and (b) represent $T^* \approx 0.006$, $T_c \approx 0.072$ and $T_{cg} \approx 0.9$, with colors in purple, green, and gray respectively.

citations $T_{cg} \approx 0.9$ is estimated from the $\bar{n} - \mu$ plateau with details in the SM [55], which is also around the highest peak of the specific heat. As for the smectic order, we estimate $T_c \approx 0.072$ as the critical temperature of the translational symmetry breaking, where the density fluctuation $S^B(\pi, 0)$ reaches the maximal value. For $T < T_c$, the formation of charge order leads to a decreasing of $S^B(\pi, 0)$. This estimation of T_c is consistent with a specific heat peak and maximal value of compressibility observed around this temperature. Below T_c , the compressibility quickly vanishes, indicating the formation of an incompressible quantum liquid state.

We note that, in Fig. 3, while DMRG simulations pick a $\mathbf{q} = (\pi, 0)$ smectic pattern, there exists strong charge fluctuation in the other direction, i.e. $(0, \pi)$, which belongs to the magnetoroton excitation of the FQAH state. In our $N_y = 3$ cylinder geometry, the closest allowed momentum to the broad roton peak is $(0, \pm 2\pi/3)$. As shown in Fig. 4 (b), while $S^B(\pi, 0)$ drops with decreasing temperature, the density fluctuation at $(0, 2\pi/3)$ increases and goes to the highest value around $T^* \approx 0.006$ while the CDW order also reaches the maximum. Around T^* the specific heat shows a shoulder behavior while the compressibility drops to 0 below T^* . Therefore, the thermodynamic of FQAHs exhibit 2 low-lying temperature scales: the roton scale T^* referring to the topological crossover temperature for the onset of the quantized Hall plateau and the critical temperature of translational symmetry breaking T_c . Both of these are much lower than the charge excitation T_{cg} , which is in accordance of previous study of the energy scales of FQAH state in correlated flat-band systems [46].

Dipolar smectic metal state As shown in earlier part, for

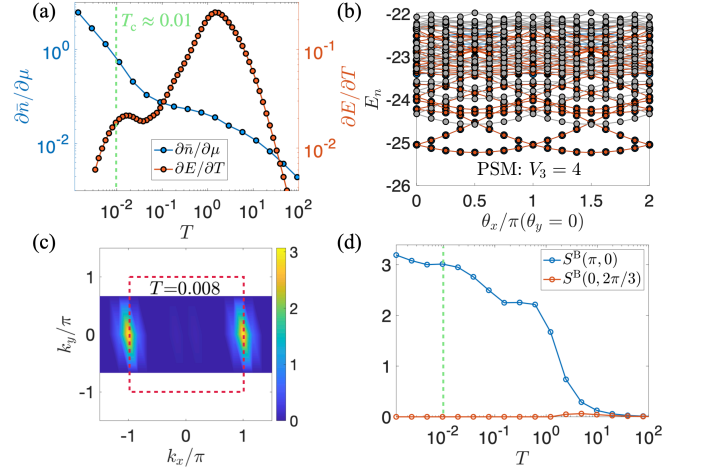


FIG. 5. **Thermodynamic behavior of polar smectic metal at $V_3 = 4$.** (a) Below $T_c \approx 0.01$ represented by the green dashed line, the specific heat roughly follows power-law behavior versus T while compressibility is non-vanishing. (b) Gapless spectrum in a $3 \times 4 \times 2$ torus with twisted boundary conditions. (c) Structure factor at $T = 0.008$. (d) Change of structure factors versus T .

$V_3 > 2.2$, the smectic order further breaks the two-fold rotational symmetry, resulting in a spontaneously generated in-plane electric dipole moment. In this phase ($V_3 = 4$), our simulations indicate that as temperature reduces towards zero, the specific heat decreases towards zero as a power-law function (with a power around unity), while the compressibility remains nonzero and increases as T is reduced. These observations clearly indicate that the dipolar smectic phase is gapless/compressible. This conclusion is further supported by ED simulations [Fig. 5(b)], where the energy spectrum under twisted boundary conditions is continuous with no gap. The thermal behavior of density fluctuations (we take B sublattice as an example) is also different from that of FQAHs. Here, the structure factor $S^B(\pi, 0)$ continues to increase at low temperature while we see no density fluctuations along k_y at low temperature as shown in Fig. 5 (c,d).

In general, charge stripe states can often be treated as coupled Luttinger liquids. Depending on microscopic details and values of control parameters, various phases have been proposed, such as smectic superconductor, smectic crystal (insulator), smectic metal, and Fermi liquid [54]. Our studies indicate that this polar smectic ordered state is gapless, and is likely to be either a smectic metal or a Fermi liquid. These two scenarios are characterized by different exponents in thermodynamic quantities, where smectic metal exhibits anomalous dimensions deviated from the Fermi liquid theory. In our simulations, the specific heat vs T function is close to linear, but the numerical resolution would not allow us to pinpoint the absence/presence of anomalous dimensions.

This observation of the polar smectic metal at large V_3 without Chern number, supports the early proposal that FQAH can coexist with partially polarized stripe state, but when the CDW order becomes strong, the FQH effect vanishes [3].

Experimentally, it will be highly interesting to probe the anisotropy and ferroelectric order induced by this polar smectic phase in the transport measurements.

Discussions

The FQAHS states identified in this research show unique characteristics that set them apart from other coexisting states of charge order and topological order. For instance, in topological pinball fluids, a portion of the electrons form a charge-ordered crystal, while the remaining contribute to topological states. Consequently, the Hall conductivity strays from the filling factor $\sigma_{xy} \neq \nu$ [45]. However, in the FQAHS states that we report, $\sigma_{xy} = \nu$ indicating that all electrons take part in forming the stripe order and, simultaneously, contribute to the FQAH effect. One conceptual way to understand these FQAHS states starts with a FQAH state without any charge order with $\sigma_{xy} = \nu$, and then perturbatively turning on the charge order. Because the FQAH effect and σ_{xy} remains robust against any perturbations, here we obtain a FQAHS state with $\sigma_{xy} = \nu$. We postulate that the FQAHS state observed in our numerical simulations is adiabatically connected to the ground state of this perturbative picture. To verify this conjecture numerically, innovative strategies, analogous to the adiabatic path demonstrated in Ref. [56], may be needed as this checkerboard-lattice model does not display a FQAH phase at the same filling without charge order. This would be an intriguing extension for future studies.

Because our FQAHS state shares the same Hall conductivity as conventional FQAH states (without charge order), current experimental studies of FQAH states, mainly focusing on directly or indirectly measuring σ_{xy} , cannot differentiate these two types of states. Thus, it is not totally impossible that some of the reported FQAH states might actually fall under the FQAHS category or something similar. Two experimental probes could provide significant insights to distinguish FQAHS states from FQAH states. The first is longitudinal transport. Since smectic order breaks spontaneously the rotational symmetry, it leads to anisotropy in longitudinal conductivity, thus yielding a nonzero expectation value for the nematic order parameter $(\sigma_{xx} - \sigma_{yy}) / (\sigma_{xx} + \sigma_{yy})$. At the ideal $T \rightarrow 0$ limit, this quantity is undefined due to $\sigma_{xx} = \sigma_{yy} = 0$. However, at finite temperature, this ratio provides hints about the existence or absence of smectic order. Because this order parameter is unaffected by the breaking of translational symmetry, it cannot distinguish between FQAH nematic and FQAH smectic states. The definitive proof of FQAHS order should involve measurements capable of probing the ordering wavevector, such as X-ray scatterings, and/or real-space imaging methods, such as scanning tunneling microscopy (STM).

Besides the topological states, the gapless polar smectic state also exhibits intriguing physical properties. This state shares the same superlattice peak as ordinary charge smectic order, but this order also generates spontaneously a nonzero electric dipole moment. Given that various charged ordered states have been reported in flat-band systems, our study implies that it is possible that some of these charged ordered states might belong to this category of polar smectic order.

Most importantly, our simulations indicate that topological flat-bands could potentially serve as a platform to realize and to explore the interplay and competition between the polar smectic order and FQAHS states.

Methods

For the ground state calculations, we employ exact diagonalization (ED) [57, 58] and density matrix renormalization group (DMRG) [59, 60] with the particle number fixed. We have used lattice translational symmetry and parallel computing to accelerate the ED calculations with the tori up to 36 lattice sites. In the DMRG calculations, we use cylinders from $N_y = 3$ to $N_y = 6$ for ground-state simulations, where N_y / N_x the number of unit cell along $\mathbf{a}_1/\mathbf{a}_2$ direction. Then we denote the total number of lattice sites as $N = N_y \times N_x \times 2$, the average density as \bar{n} and the filling of the lower flat band ν as $\bar{n} = N_e/N = \nu/2$. While for finite-temperature simulations, we work in the grand canonical ensemble in exponential tensor renormalization groups (XTRG) [61] by including the chemical potential term $H_\mu = \mu \sum_i (\hat{n}_i - \frac{1}{2})$ to tune the particle number $N_e = \sum_i \langle \hat{n}_i \rangle_\beta$ (here, $\langle \cdot \rangle_\beta$ denotes the ensemble average at inverse temperature $\beta \equiv \frac{1}{T}$). The charge gap Δ_{cg} is estimated by the average change of H_μ to add or subtract a particle in the system. For thermal simulations, we mainly use $N_y = 3$ cylinder in XTRG calculations. The DMRG and XTRG simulations are based on the QSpace framework [62] with U(1) symmetry and complex numbers, and the bond dimensions are up to $D = 2048$ and $D = 800$ respectively.

Acknowledgements

We thank Cenke Xu, Bo Yang and Todadri Senthil for helpful discussions. HYL, BBC and ZYM acknowledge the support from the Research Grants Council (RGC) of Hong Kong Special Administrative Region of China (Project Nos. 17301721, AoE/P-701/20, 17309822, HKU C7037-22G, 17302223), the ANR/RGC Joint Research Scheme sponsored by RGC of Hong Kong and French National Research Agency (Project No. A_HKU703/22). We thank HPC2021 system under the Information Technology Services and the Blackbody HPC system at the Department of Physics, University of Hong Kong, as well as the Beijing PARATERA Tech CO.,Ltd. (URL: <https://cloud.paratera.com>) for providing HPC resources that have contributed to the research results reported within this paper. H.Q. Wu acknowledges the support from Guangdong Provincial Key Laboratory of Magnetoelectric Physics and Devices (No. 2022B1212010008) and Guangzhou Basic and Applied Basic Research Foundation (No. 202201011569).

* The two authors contributed equally to this work.

† bchenhku@hku.hk

‡ sunkai@umich.edu

§ zymeng@hku.hk

[1] S. Kivelson, C. Kallin, D. P. Arovas, and J. R. Schrieffer, *Phys. Rev. Lett.* **56**, 873 (1986).

- [2] B. I. Halperin, Z. Tešanović, and F. Axel, *Phys. Rev. Lett.* **57**, 922 (1986).
- [3] Z. Tešanović, F. m. c. Axel, and B. I. Halperin, *Phys. Rev. B* **39**, 8525 (1989).
- [4] L. Balents, *Europhysics Letters* **33**, 291 (1996).
- [5] E. Fradkin and S. A. Kivelson, *Phys. Rev. B* **59**, 8065 (1999).
- [6] G. Murthy, *Phys. Rev. Lett.* **85**, 1954 (2000).
- [7] J. Cai, E. Anderson, C. Wang, X. Zhang, X. Liu, W. Holtzmann, Y. Zhang, F. Fan, T. Taniguchi, K. Watanabe, Y. Ran, T. Cao, L. Fu, D. Xiao, W. Yao, and X. Xu, *Nature* **622**, 63 (2023).
- [8] H. Park, J. Cai, E. Anderson, Y. Zhang, J. Zhu, X. Liu, C. Wang, W. Holtzmann, C. Hu, Z. Liu, T. Taniguchi, K. Watanabe, J.-H. Chu, T. Cao, L. Fu, W. Yao, C.-Z. Chang, D. Cobden, D. Xiao, and X. Xu, *Nature* **622**, 74 (2023).
- [9] Y. Zeng, Z. Xia, K. Kang, J. Zhu, P. Knüppel, C. Vaswani, K. Watanabe, T. Taniguchi, K. F. Mak, and J. Shan, *Nature* **622**, 69 (2023).
- [10] F. Xu, Z. Sun, T. Jia, C. Liu, C. Xu, C. Li, Y. Gu, K. Watanabe, T. Taniguchi, B. Tong, J. Jia, Z. Shi, S. Jiang, Y. Zhang, X. Liu, and T. Li, *Phys. Rev. X* **13**, 031037 (2023).
- [11] Z. Lu, T. Han, Y. Yao, A. P. Reddy, J. Yang, J. Seo, K. Watanabe, T. Taniguchi, L. Fu, and L. Ju, Fractional quantum anomalous hall effect in a graphene moire superlattice (2023), [arXiv:2309.17436 \[cond-mat.mes-hall\]](https://arxiv.org/abs/2309.17436).
- [12] D. G. Barci, E. Fradkin, S. A. Kivelson, and V. Oganesyan, *Phys. Rev. B* **65**, 245319 (2002).
- [13] D. G. Barci and E. Fradkin, *Phys. Rev. B* **65**, 245320 (2002).
- [14] G. Murthy, *Phys. Rev. Lett.* **84**, 350 (2000).
- [15] C.-C. Chang, C. Töke, G. S. Jeon, and J. K. Jain, *Phys. Rev. B* **73**, 155323 (2006).
- [16] Z.-W. Zuo, A. C. Balram, S. Pu, J. Zhao, T. Jolicœur, A. Wójs, and J. K. Jain, *Phys. Rev. B* **102**, 075307 (2020).
- [17] G. A. Csáthy, D. C. Tsui, L. N. Pfeiffer, and K. W. West, *Phys. Rev. Lett.* **92**, 256804 (2004).
- [18] H. Zhu, Y. P. Chen, P. Jiang, L. W. Engel, D. C. Tsui, L. N. Pfeiffer, and K. W. West, *Phys. Rev. Lett.* **105**, 126803 (2010).
- [19] J. Xia, J. P. Eisenstein, L. N. Pfeiffer, and K. W. West, *Nature Physics* **7**, 845 (2011).
- [20] L. Du, U. Wurstbauer, K. W. West, L. N. Pfeiffer, S. Fallahi, G. C. Gardner, M. J. Manfra, and A. Pinczuk, *Science Advances* **5**, eaav3407 (2019).
- [21] X. Fu, Q. Shi, M. A. Zudov, G. C. Gardner, J. D. Watson, M. J. Manfra, K. W. Baldwin, L. N. Pfeiffer, and K. W. West, *Phys. Rev. Lett.* **124**, 067601 (2020).
- [22] N. Samkharadze, K. A. Schreiber, G. C. Gardner, M. J. Manfra, E. Fradkin, and G. A. Csáthy, *Nature Physics* **12**, 191 (2016).
- [23] J. Jang, B. M. Hunt, L. N. Pfeiffer, K. W. West, and R. C. Ashoori, *Nature Physics* **13**, 340 (2017).
- [24] H. Q. Trung and B. Yang, *Phys. Rev. Lett.* **127**, 046402 (2021).
- [25] V. Shingla, H. Huang, A. Kumar, L. N. Pfeiffer, K. W. West, K. W. Baldwin, and G. A. Csáthy, *Nature Physics* **19**, 689 (2023).
- [26] F. D. M. Haldane, *Phys. Rev. Lett.* **61**, 2015 (1988).
- [27] K. Sun, Z. Gu, H. Katsura, and S. Das Sarma, *Phys. Rev. Lett.* **106**, 236803 (2011).
- [28] D. Sheng, Z.-C. Gu, K. Sun, and L. Sheng, *Nature Communications* **2**, 389 (2011).
- [29] T. Neupert, L. Santos, C. Chamon, and C. Mudry, *Phys. Rev. Lett.* **106**, 236804 (2011).
- [30] C.-Z. Chang, J. Zhang, X. Feng, J. Shen, Z. Zhang, M. Guo, K. Li, Y. Ou, P. Wei, L.-L. Wang, Z.-Q. Ji, Y. Feng, S. Ji, X. Chen, J. Jia, X. Dai, Z. Fang, S.-C. Zhang, K. He, Y. Wang, L. Lu, X.-C. Ma, and Q.-K. Xue, *Science* **340**, 167 (2013), <https://www.science.org/doi/pdf/10.1126/science.1234414>.
- [31] H. Li, U. Kumar, K. Sun, and S.-Z. Lin, *Phys. Rev. Res.* **3**, L032070 (2021).
- [32] V. Crépel and L. Fu, *Phys. Rev. B* **107**, L201109 (2023).
- [33] J. Dong, J. Wang, P. J. Ledwith, A. Vishwanath, and D. E. Parker, *Phys. Rev. Lett.* **131**, 136502 (2023).
- [34] H. Goldman, A. P. Reddy, N. Paul, and L. Fu, *Phys. Rev. Lett.* **131**, 136501 (2023).
- [35] C. Xu, J. Li, Y. Xu, Z. Bi, and Y. Zhang, (2023), [arXiv:2308.09697 \[cond-mat.str-el\]](https://arxiv.org/abs/2308.09697).
- [36] J. Yu, J. Herzog-Arbeitman, M. Wang, O. Vafek, B. A. Bernevig, and N. Regnault, Fractional chern insulators vs. non-magnetic states in twisted bilayer mote₂ (2023), [arXiv:2309.14429 \[cond-mat.mes-hall\]](https://arxiv.org/abs/2309.14429).
- [37] A. P. Reddy, F. Alsallom, Y. Zhang, T. Devakul, and L. Fu, *Phys. Rev. B* **108**, 085117 (2023).
- [38] C. Wang, X.-W. Zhang, X. Liu, Y. He, X. Xu, Y. Ran, T. Cao, and D. Xiao, Fractional chern insulator in twisted bilayer mote₂ (2023), [arXiv:2304.11864 \[cond-mat.str-el\]](https://arxiv.org/abs/2304.11864).
- [39] X.-Y. Song and T. Senthil, Density wave halo around anyons in fractional quantum anomalous hall states (2023), [arXiv:2311.16216 \[cond-mat.str-el\]](https://arxiv.org/abs/2311.16216).
- [40] X.-Y. Song, Y.-H. Zhang, and T. Senthil, [arXiv e-prints](https://arxiv.org/abs/2308.10903), [arXiv:2308.10903 \[cond-mat.str-el\]](https://arxiv.org/abs/2308.10903).
- [41] B. Zhou, H. Yang, and Y.-H. Zhang, Fractional quantum anomalous hall effects in rhombohedral multilayer graphene in the moiréless limit and in coulomb imprinted superlattice (2023), [arXiv:2311.04217 \[cond-mat.str-el\]](https://arxiv.org/abs/2311.04217).
- [42] J. Dong, T. Wang, T. Wang, T. Soejima, M. P. Zaletel, A. Vishwanath, and D. E. Parker, Anomalous hall crystals in rhombohedral multilayer graphene i: Interaction-driven chern bands and fractional quantum hall states at zero magnetic field (2023), [arXiv:2311.05568 \[cond-mat.str-el\]](https://arxiv.org/abs/2311.05568).
- [43] Y. H. Kwan, J. Yu, J. Herzog-Arbeitman, D. K. Efetov, N. Regnault, and B. A. Bernevig, [arXiv e-prints](https://arxiv.org/abs/2312.11617), [arXiv:2312.11617 \[cond-mat.str-el\]](https://arxiv.org/abs/2312.11617).
- [44] X.-Y. Song, C.-M. Jian, L. Fu, and C. Xu, Intertwined fractional quantum anomalous hall states and charge density waves (2023), [arXiv:2310.11632 \[cond-mat.str-el\]](https://arxiv.org/abs/2310.11632).
- [45] S. Kourtis and M. Daghofer, *Phys. Rev. Lett.* **113**, 216404 (2014).
- [46] H. Lu, B.-B. Chen, H.-Q. Wu, K. Sun, and Z. Y. Meng, Thermodynamic response and neutral excitations in integer and fractional quantum anomalous hall states emerging from correlated flat bands (2023), [arXiv:2311.15246 \[cond-mat.str-el\]](https://arxiv.org/abs/2311.15246).
- [47] X. Chen, V. Martinez, P. Nacke, E. Korblova, A. Manabe, M. Klasen-Memmer, G. Freychet, M. Zhernenkov, M. A. Glaser, L. Radzihovsky, J. E. MacLennan, D. M. Walba, M. Bremer, F. Giesselmann, and N. A. Clark, *Proceedings of the National Academy of Sciences* **119**, e2210062119 (2022), <https://www.pnas.org/doi/pdf/10.1073/pnas.2210062119>.
- [48] L. Nie, G. Tarjus, and S. A. Kivelson, *Proceedings of the National Academy of Sciences* **111**, 7980 (2014).
- [49] R. M. Fernandes, P. P. Orth, and J. Schmalian, *Annual Review of Condensed Matter Physics* **10**, 133 (2019).
- [50] Y.-C. Wang, Z. Yan, C. Wang, Y. Qi, and Z. Y. Meng, *Phys. Rev. B* **103**, 014408 (2021).
- [51] Z. Sun, G. Ye, M. Huang, C. Zhou, N. Huang, Q. Li, Z. Ye, C. Nnokwe, H. Deng, D. Mandrus, Z. Y. Meng, K. Sun, C. Du, R. He, and L. Zhao, [arXiv e-prints](https://arxiv.org/abs/2311.03493), [arXiv:2311.03493 \(2023\)](https://arxiv.org/abs/2311.03493), [arXiv:2311.03493 \[cond-mat.mtrl-sci\]](https://arxiv.org/abs/2311.03493).
- [52] N. Francini and L. Janssen, [arXiv e-prints](https://arxiv.org/abs/2311.08475), [arXiv:2311.08475 \(2023\)](https://arxiv.org/abs/2311.08475), [arXiv:2311.08475 \[cond-mat.str-el\]](https://arxiv.org/abs/2311.08475).
- [53] S. A. Kivelson, E. Fradkin, and V. J. Emery, *Nature* **393**, 550 (1998).

- [54] V. J. Emery, E. Fradkin, S. A. Kivelson, and T. C. Lubensky, *Phys. Rev. Lett.* **85**, 2160 (2000).
- [55] We provide supplementary ED results in Section I and more detailed finite-temperature structure factor of FQAHS phase in Section II. Moreover, we show supplementary thermodynamic data of FQAHS and PSM phases in Section III and Section IV, respectively. The degenerate stripe patterns are shown in Section V. In addition, the order parameters, symmetry analysis and the Ginzburg-Landau theory of smectic phases are shown in Section. VI.
- [56] Y.-H. Wu, J. K. Jain, and K. Sun, *Phys. Rev. B* **86**, 165129 (2012).
- [57] A. W. Sandvik, *AIP Conference Proceedings* **1297**, 135 (2010), https://pubs.aip.org/aip/acp/article-pdf/1297/1/135/11407753/135_1_online.pdf.
- [58] A. M. Läuchli, Numerical simulations of frustrated systems, in *Introduction to Frustrated Magnetism: Materials, Experiments, Theory*, edited by C. Lacroix, P. Mendels, and F. Mila (Springer Berlin Heidelberg, Berlin, Heidelberg, 2011) pp. 481–511.
- [59] S. R. White, *Phys. Rev. Lett.* **69**, 2863 (1992).
- [60] U. Schollwöck, *Rev. Mod. Phys.* **77**, 259 (2005).
- [61] B.-B. Chen, L. Chen, Z. Chen, W. Li, and A. Weichselbaum, *Phys. Rev. X* **8**, 031082 (2018).
- [62] A. Weichselbaum, *Annals of Physics* **327**, 2972 (2012).
- [63] Q. Niu, D. J. Thouless, and Y.-S. Wu, *Phys. Rev. B* **31**, 3372 (1985).
- [64] C. N. Varney, K. Sun, M. Rigol, and V. Galitski, *Phys. Rev. B* **84**, 241105 (2011).
- [65] T. Fukui, Y. Hatsugai, and H. Suzuki, *Journal of the Physical Society of Japan* **74**, 1674 (2005), <https://doi.org/10.1143/JPSJ.74.1674>.

SUPPLEMENTAL MATERIAL FOR
FROM FRACTIONAL QUANTUM ANOMALOUS HALL SMECTICS TO POLAR SMECTIC METALS: NONTRIVIAL INTERPLAY BETWEEN ELECTRONIC LIQUID CRYSTAL ORDER AND TOPOLOGICAL ORDER IN CORRELATED TOPOLOGICAL FLAT BANDS

We provide supplementary ED results in Section I and more detailed finite-temperature structure factor of FQAHS phase in Section II. Moreover, we show supplementary thermodynamic data of FQAHS and PSM phases in Section III and Section IV, respectively. The degenerate stripe patterns are shown in Section V. In addition, the order parameters, symmetry analysis and the Ginzburg-Landau theory of smectic phases are shown in Section. VI.

Section I: Supplementary ED results

Throughout the main text and SM, the ED simulations of Chern numbers are based on the following formula first proposed in Ref. 63. More details on implementation can be found in Ref. 64 and 65.

$$C = \frac{i}{2\pi} \int \int d\phi_1 d\phi_2 \left[\frac{\partial}{\partial \phi_1} \langle \Omega(\phi_1, \phi_2) | \frac{\partial}{\partial \phi_2} | \Omega(\phi_1, \phi_2) \rangle - \frac{\partial}{\partial \phi_2} \langle \Omega(\phi_1, \phi_2) | \frac{\partial}{\partial \phi_1} | \Omega(\phi_1, \phi_2) \rangle \right]. \quad (\text{S1})$$

In the main text, we have shown the energy spectra on $3 \times 6 \times 2$ torus in Fig.2(a), and here we show the spectra on $3 \times 4 \times 2$ torus in Fig.S1(a). The momentum points in the Brillouin zone for two system sizes are shown in Fig.S1(b) and Fig.S1(c), respectively.

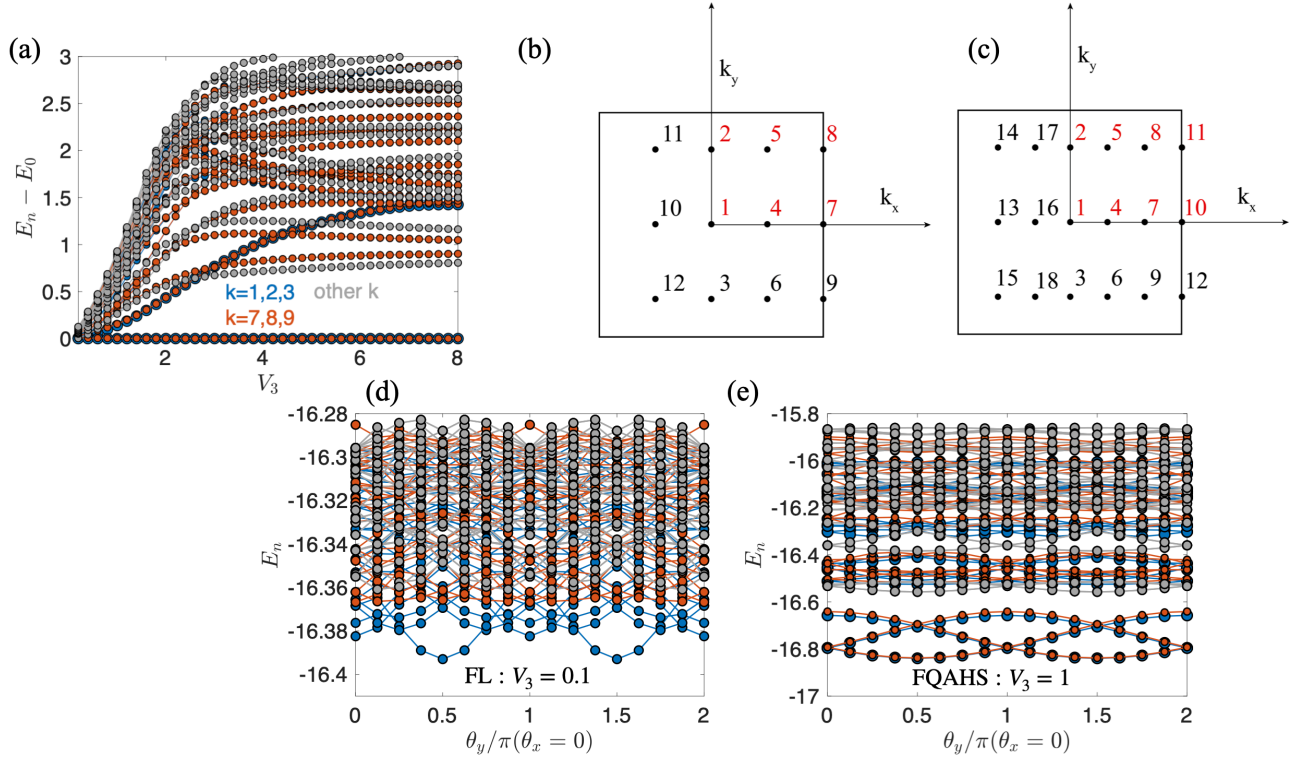


FIG. S1. (a) Energy spectra of a $3 \times 4 \times 2$ torus with changing V_3 . We use four different colors to represent these energy levels, where light blue points represent the energy levels from momentum sectors labeling $k = 1, 2, 3$, the red color points represent the energy levels from $k = 7, 8, 9$, while the energy levels from other k are represented with gray color. (b) and (c) show the momentum points in the Brillouin zone of the $3 \times 4 \times 2$ and $3 \times 6 \times 2$ torus, respectively. The energy spectra of momentum sectors marked by red color are simulated using Lanczos, while the black ones can be obtained by mirror or rotational point-group symmetry. (d-e) Energy spectrum flow of FL, and FQAHS phases and twist boundary conditions using a $3 \times 4 \times 2$ torus. The colors are the same as those of (a).

While we have shown the gapped spectrum of FQAHs phase on a $3 \times 6 \times 2$ torus in Fig.3(c), we show here the spectrum flow of FL and FQAHs phase on a $3 \times 4 \times 2$ in Fig.S1(d-e).

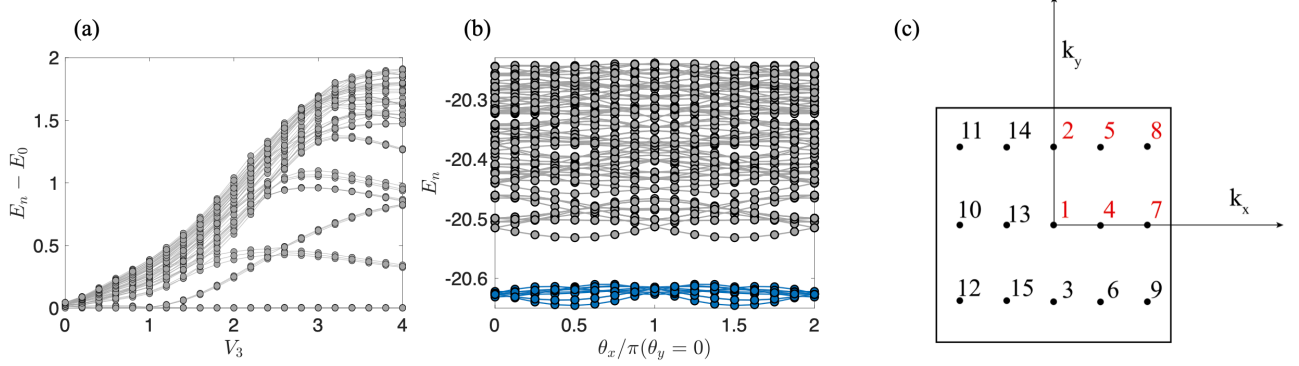


FIG. S2. (a) Energy spectrum of a $3 \times 5 \times 2$ torus with changing V_3 . (b) Spectrum flow with $V_3 = 1$ and twisted boundary conditions. The blue ones represent the 15-fold degenerate ground states, consisting of the lowest energy level of each momentum sector define in (c).

Since the Bragg peak of the density density correlation function in the FQAHs phase are either $(\pm\pi, 0)$ or $(0, \pm\pi)$, the $3 \times 5 \times 2$ torus are not the suitable geometry for the charge-smectic order along any direction. However, we will show that the incompatible geometry does not change the topological nature. Here, We show the spectra of 30 sites torus in Fig.S2(a), and the spectra flow at $V_3 = 1$ in Fig.S2(b). In the cases of 24 and 36 sites, the ground-state degeneracy is $6 = 3 \times 2$. While in the case of 30 sites without $(\pm\pi, 0)$ momentum points, the ground-state degeneracy is $15 = 3 \times 5$ (L_y), and each momentum sector shown in Fig.S2(c) contributes one ground state. When calculating the Chern number of each state using Eq.S1 with ϕ_1 (ϕ_2) from 0 to 2π , the Chern number of each states is still $2/3$, in agreement with the results of FQAHs phase in the main text.

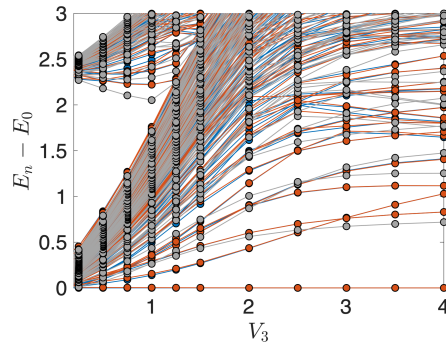


FIG. S3. Spectra on a $3 \times 4 \times 2$ torus with 60 energy levels consider at each momentum sector and the definition of color is the same as that in Fig.S1(a).

While in the previous spectra in Fig.S1(a), we consider only 10 energy levels in each momentum sector, here we show the ED spectra with around 60 energy levels in Fig.S3. It is clear that, while the energy levels from the remote band are not playing a role in FL phase, they quickly merge into the intermediate-energy levels and are playing a role in the FQAHs and PSM phases.

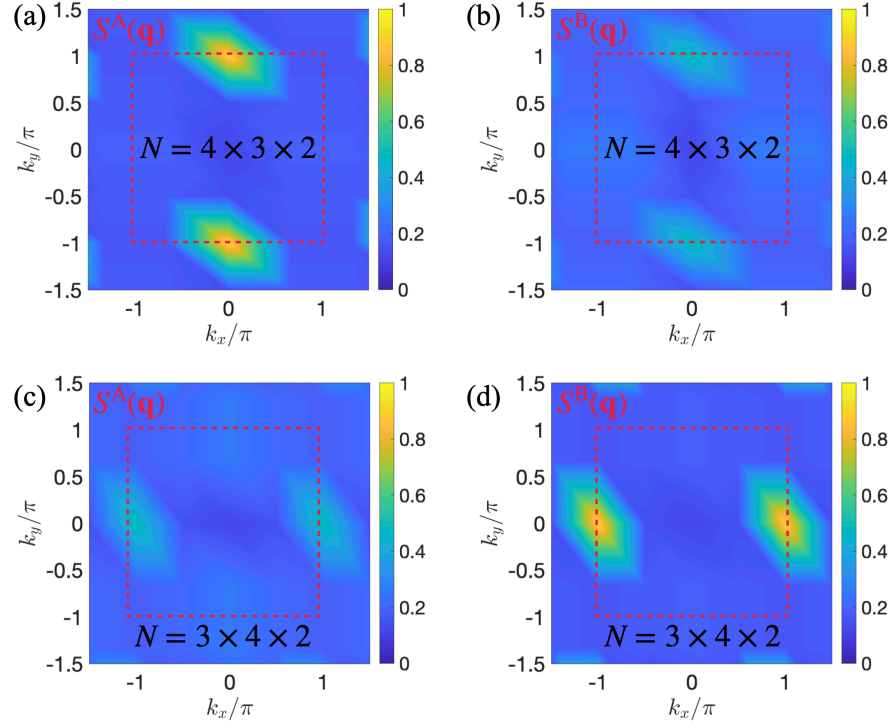


FIG. S4. The structure factors of A and B sublattices in FQAHS state with $V_3 = 1$ and different geometries, respectively.

In the main text, we have shown that in the intermediate FQAHS phase, there is large difference in the charge-smectic order between the sublattices. Here, we also plot the ED structure factors of $V_3 = 1$ with different geometries in Fig.S4. In the $N = 3 \times 4 \times 2$ torus, the smectic order is along the N_x direction and that of B sublattice is much stronger than that of A sublattice. However, the results in $N = 4 \times 3 \times 2$ torus totally reverse. This supports our analysis in the main text.

Section II: Detailed finite-temperature structure factors of FQAHS phase

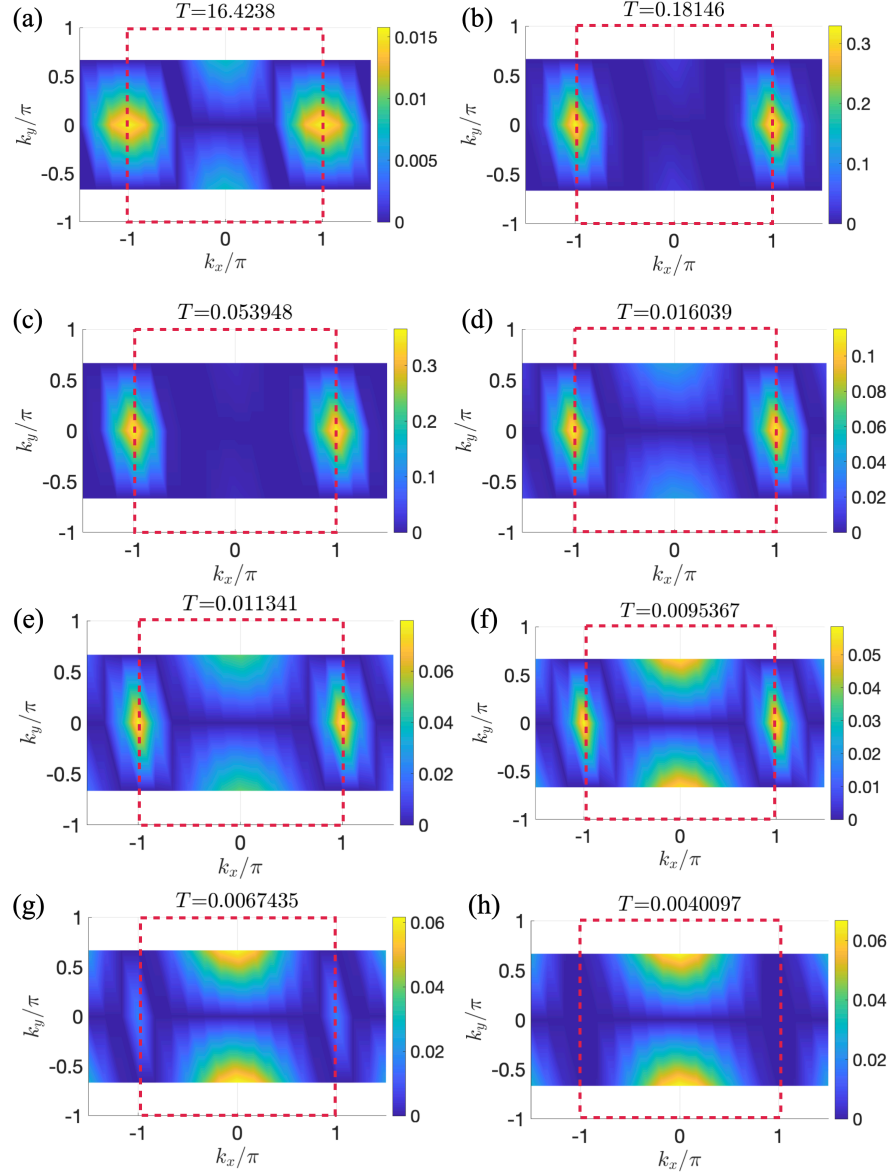


FIG. S5. Detailed structure factor in FQAHS state with $V_3 = 1$ from high to low temperature.

In Fig.3 of main text, we have shown that in FQAHS state, when the peaks of $n(\mathbf{k})$ are at $(\pm\pi, 0)$, the broad peaks of density fluctuation are at $(0, \pm\pi)$, which are the rotons. In the thermodynamic results of FQAHS, we have shown that around T_c (the transition temperature of spontaneously breaking translational symmetry), the structure factor $S(\pm\pi, 0)$ goes to the peak and will drop to 0 when approaching the ground state at lower temperature. Meanwhile, since the geometry of our XTRG simulations does not include $\mathbf{k} = (0, \pm\pi)$, we examine $S(0, 2\pi/3)$ instead for the roton excitation, and it quickly establishes when $T < T_c$ and finally approaches the constant value around T^* . In the main text, the finite-temperature structure factors are only plotted at two distinct temperature values, so we show more detailed figures of the structure factor of the FQAHS state with $V_3 = 1$ in Fig.S5

Section III: Supplementary thermodynamic data of FQAHS phase

Here, we show the supplementary thermodynamic data of FQAHS phase with $V_3 = 1$ in Fig.S6. We obtain the estimated $\Delta_{\text{cg}} \approx 0.9$ from the $\bar{n} - \mu$ plateau, which is roughly the T_{cg} of this phase. And it is in agreement with the analysis in the main text that the thermal entropy approaches 0 under the onset temperature T^* , but is still finite around T_c .

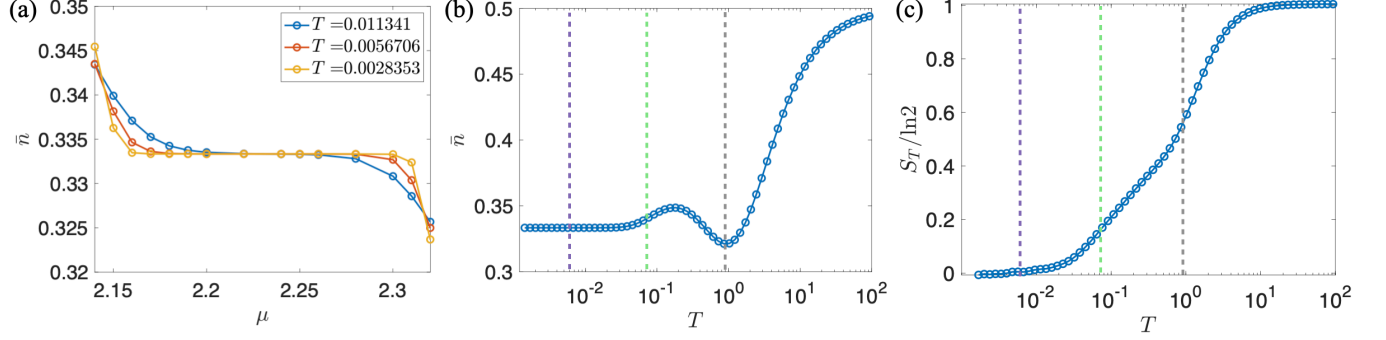


FIG. S6. Supplementary thermodynamic data with $V_3 = 1$. (a) $\bar{n} - \mu$ plateau and the estimated charge gap is $\Delta_{\text{cg}} \approx 0.9$. Change of average density (b) and thermal entropy (c) versus T. The definitions of dashed lines are the same as Fig.4.

Section IV: Supplementary thermodynamic data of PSM phase

Here, we show the supplementary thermodynamic data of PSM phase with $V_3 = 4$ in Fig.S7. The gapless nature is again shown in Fig.S7(a), in agreement with the compressibility in Fig.5 (b), and the thermal entropy is still finite, which further supports the metallic ground state.

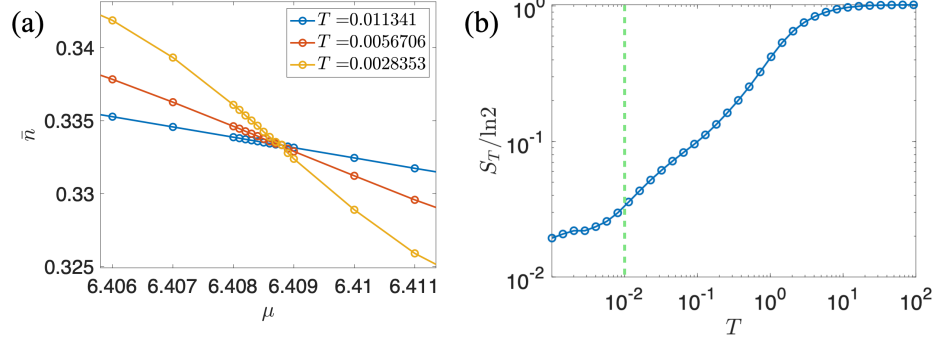


FIG. S7. Supplementary thermodynamic data with $V_3 = 4$. (a) $\bar{n} - \mu$ curve without plateau. (b) Change of thermal entropy versus T. The definition of dashed line is the same as Fig.5.

Section V: Degenerate stripe patterns

In the main text, we showed that the PSM state has a dipolar stripe order. Here we present the 4 degenerate charge patterns of this polar smectic order for stripes along the \mathbf{a}_1 direction. In the thermodynamic limit, the degeneracy is 8-fold, when additional 4 ground states with stripes along \mathbf{a}_2 is taken into account.

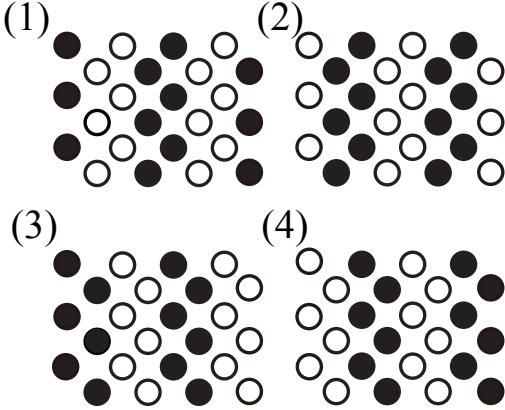


FIG. S8. Four degenerate polar stripe patterns along \mathbf{a}_1 direction. Fluctuating intertwined stripes in the strange metal regime of the Hubbard model

Section VI: Order parameters, symmetry analysis and the Ginzburg-Landau theory of smectic phases

In this section, we analyze the symmetry breaking patterns for various stripe orders in this checkerboard lattice model, and show that this model support two different types of smectic states, polar and non-polar. In addition, we will also present the order parameters for these two different smectic orders.

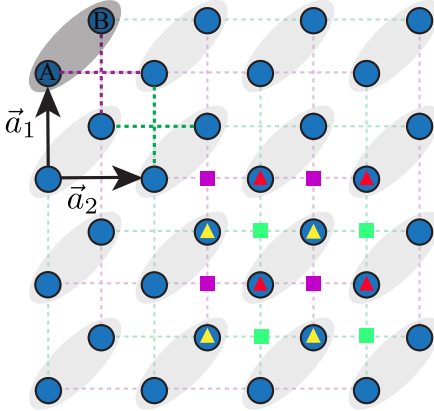


FIG. S9. Space group symmetry of the checkerboard lattice model P4 (442). In the absence of any charge order, in each unit cell, there are two 4-fold rotation center (purple and green squares) and two 2-fold rotation center (yellow and red triangles).

For a checkerboard lattice, it turns out that to achieve this goal we need to take into account the full space-symmetry group, instead of treating translational symmetry breaking and rotational symmetry breaking separately. The 2D space group (known as the wallpaper group) of a naive checkerboard lattice is $p4m$ (*442). However, in our model, because the reflection and gliding-reflection symmetries are broken by the loop current pattern, the space group is reduced to P4 (442). As shown in Fig. S9, in each unit cell, this model has two 4-fold rotation center (purple and green squares) and two 2-fold rotation center (yellow and red triangles).

We start from nonpolar stripe orders. For a nonpolar stripe order with ordering wavevector $(\pi, 0)$ or $(0, \pi)$, it breaks the 4-fold rotational symmetry down to two-fold. Although this naive statement on rotational symmetry breaking pattern is fully correct, as far as the point group symmetry is concerned, the full story of symmetry breaking is more complicated, once we taken into account the space symmetry group. In reality, this is what happened for the two 4-fold rotation center and two 2-fold rotation center: (1) the stripe pattern removes one 4-fold rotational center and one 2-fold rotation center; (2) the other 2-fold rotation center remains; (3) the other 4-fold rotation center becomes a 2-fold center.

To better demonstrate this symmetry breaking pattern, here we define four charge stripe order parameters

$$\delta_x^A = \frac{2}{N} \sum_i (-1)^{x_i} n_{\mathbf{r}_i}^A \quad (\text{S2})$$

$$\delta_x^B = \frac{2}{N} \sum_i (-1)^{x_i} n_{\mathbf{r}_i}^B \quad (\text{S3})$$

and

$$\delta_y^A = \frac{2}{N} \sum_i (-1)^{y_i} n_{\mathbf{r}_i}^A \quad (\text{S4})$$

$$\delta_y^B = \frac{2}{N} \sum_i (-1)^{y_i} n_{\mathbf{r}_i}^B \quad (\text{S5})$$

where i labels unit cells and $\mathbf{r}_i = (x_i, y_i)$ is the 2D coordinate of the unit cell. Because we set the lattice constant to be unity, x_i and y_i are both integers. $n_{\mathbf{r}_i}^A$ and $n_{\mathbf{r}_i}^B$ are average density on site A and site B respectively. The first two order parameters δ_x^A and δ_x^B describes stripes along y (ordering wavevector along x), while the last two order parameters δ_y^A and δ_y^B describes stripes along x (ordering wavevector along y). The superscript A or B indicates whether the charge density wave is from sublattice A or B.

Here, for simplicity, we will focus on stripes orders characterized by δ_x^A and δ_x^B , setting $\delta_y^A = \delta_y^B = 0$. The same conclusions also apply to stripe orders of δ_y^A and δ_y^B via a simple 90° rotation. One crucial symmetry property of the checkerboard lattice lies in the fact that order parameters δ_x^A and δ_x^B breaks different symmetry and thus they corresponds to two totally different stripe orders:

1. if $\delta_x^A \neq 0$ and $\delta_x^B = 0$, i.e., stripe on sublattice A only, the 4-fold rotation center marked by a green square becomes a 2-fold rotation center, the 2-fold rotation center marked by a red triangle remains, and the other two rotation centers are no longer rotation centers anymore.
2. if $\delta_x^A = 0$ and $\delta_x^B \neq 0$, i.e., stripe on sublattice B only, the 4-fold rotation center marked by a purple square becomes a 2-fold rotation center, the 2-fold rotation center marked by a yellow triangle remains, and the other two rotation centers are no longer rotation centers anymore.

Note that although these two stripe ordered states share the same point group (C_2), their rotational center are totally different. Thus, when space group symmetry is taken into account. These two order parameters breaks totally different symmetry and thus they defines two different stripe order with distinct symmetry. It is also worthwhile to emphasize that these two order parameters δ_x^A and δ_x^B are *not* connected by any symmetry, and thus it is allowed by symmetry for the system to develop one order but not the other.

What if both δ_x^A and δ_x^B becomes nonzero? For $\delta_x^A \neq 0$ and $\delta_x^B \neq 0$, the system breaks all rotational symmetry, and there is no rotation center any more in this ordered state. Because all point group symmetry is broken, an electric dipole moment becomes allowed, and thus the system becomes a polar smectic state with a spontaneously generated ferroelectric order. The ferroelectric order parameter is $\delta_x^A \times \delta_x^B$, which is nonzero only if both δ_x^A and δ_x^B become nonzero.

Here we summarize all possible stripe orders (for stripes along y) in this table

| | $\delta_x^A = 0$ | $\delta_x^A \neq 0$ |
|---------------------|--|--|
| $\delta_x^B = 0$ | disorder | nonpolar smectic (2-fold rotation centers: green square and red triangle) |
| $\delta_x^B \neq 0$ | nonpolar smectic (2-fold rotation centers: purple square and yellow triangle) | polar smectic order (no rotation centers) |

With this symmetry knowledge, we can now write down the Ginzburg-Landau theory for such stripe phases. The Ginzburg-Landau free energy is

$$F = m_1[(\delta_x^A)^2 + (\delta_y^B)^2] + m_2[(\delta_x^B)^2 + (\delta_y^A)^2] + \text{higher order terms.} \quad (\text{S6})$$

The higher order terms include quartic terms of δ 's and beyond. They give energy penalty to states with both δ_x and δ_y being nonzero, and thus we only see stripe pattern with enlarged unit cells of 2×1 or 1×2 . Because a 90° rotation swaps A and B, as well as x and y , the four fold rotational symmetry enforces a symmetry between δ_x^A and δ_y^B , as well as between δ_x^B and δ_y^A . Thus, we have only two independent quadratic coefficients m_1 and m_2 .

At small V_3 ($V_3 < 0.2$), both m_1 and m_2 are large and positive, and thus the disordered phase (all δ 's being zero) is favored. As V_3 increases, the values of both m_1 and m_2 reduce towards zero and eventually triggers a quantum phase transition. Our simulation indicates that m_2 is likely to be smaller than m_1 and thus, the phase transition first leads to a nonpolar smectic order ($0.2 < V_3 < 2.2$): either $\delta_x^B \neq 0$ or $\delta_y^A \neq 0$ (i.e., B-site stripes along y or A-site stripes along x). Depending on the signs of the order parameter (positive or negative), we have four degenerate charge patterns. In our systems, due to the 3-fold topological degeneracy, the total ground state degeneracy is 12-fold.

Upon further increasing V_3 , both m_1 and m_2 become either negative or smaller enough, which triggers a second phase transition $V_3 > 2.2$. In this phase, the ground states have both $\delta_x^A \neq 0$ and $\delta_x^B \neq 0$ (or both $\delta_y^A \neq 0$ and $\delta_y^B \neq 0$). For stripes along y we have two nonzero order parameters, δ_x^A and δ_x^B , their signs can be $(++)$, $(-)$, $(+-)$ and $(-+)$, giving us four degenerate ground states. In addition, another four degenerate ground states can be found for stripes along x , making total degeneracy 8-fold.

To conclude this section, we introduce another sets of stripe order parameters for bond stripe order

$$b_x^A = \frac{2}{N} \sum_i (-1)^{x_i} |\langle c_{A,r_i}^\dagger c_{A,r_i+(1,0)}^\dagger \rangle| \quad (S7)$$

$$b_x^B = \frac{2}{N} \sum_i (-1)^{x_i} |\langle c_{B,r_i}^\dagger c_{B,r_i+(1,0)}^\dagger \rangle| \quad (S8)$$

and

$$b_y^A = \frac{2}{N} \sum_i (-1)^{x_i} |\langle c_{A,r_i}^\dagger c_{A,r_i+(0,1)}^\dagger \rangle| \quad (S9)$$

$$b_y^B = \frac{2}{N} \sum_i (-1)^{x_i} |\langle c_{B,r_i}^\dagger c_{B,r_i+(0,1)}^\dagger \rangle| \quad (S10)$$

It is easy to check that δ^A and b^B break the same symmetry and thus they describe the same stripe order, while δ^B and b^A break the same symmetry and describe the same stripe order.
